Improved Al-Mg alloy surface segregation predictions with a machine learning atomistic potential

Christopher M. Andolina,[1] Jacob G. Wright,[1] Nishith Das,[2] and Wissam A. Saidi[1,*]
[1]Department of Mechanical Engineering and Materials Science, University of Pittsburgh, Pittsburgh, Pennsylvania 15216, USA
[2]National Institute of Technology, Sendai College, Natori Campus, Natori 981-1239, Japan

(Received 22 March 2021; revised 15 July 2021; accepted 30 July 2021; published xxxxxxxxxx)

Various industrial/commercial applications use Al-Mg alloys, yet the Mg added to Al materials, to improve strength, is susceptible to surface segregation and oxidation, leaving behind a softer and Al-enriched bulk alloy. To better understand this process and provide a systematic methodology for investigating dopants that can mitigate corrosion, we have developed a robust atomistic deep neural net potential (DNP) using a dataset generated with first-principles density-functional theory (DFT). The potential, validated systematically against DFT values, has been shown to have a high fidelity in calculating different elemental and intermetallic Al-Mg systems' properties. Our calculations predict a linear trend in the formation energy of the Al-Mg alloy and its density as a function of temperature, consistent with experimental literature. Employing the DNP within a hybrid Monte Carlo and molecular dynamics (MC/MD) approach, we predict anisotropic surface segregation for Al-Mg alloys such that (111)<(100)<(110), with (111) surfaces displaying the lowest segregation enthalpies and Mg enrichment. Furthermore, we model the segregation tendencies by adapting a recently introduced isotherm model for grain boundary segregation. Our results show that this model describes the MC/MD segregation profiles with higher fidelity than the McLean and Fowler-Guggenheim isotherm models.

DOI: 10.1103/PhysRevMaterials.00.003800

I. INTRODUCTION

Aluminum is the most abundant metal in the Earth's crust at ∼8.3% by weight [1,2]. Homogeneous Al materials are relatively soft, limiting their use in most engineering applications where high-strength mechanical properties are required. Doping with Mg can strengthen Al-based alloys for light-mass applications [3]. Commercial and industrial applications, such as the automotive and aerospace industries [4–8], use these strain-hardened Al-Mg alloys with a high strength-to-weight ratio as materials in vehicles.

As is true in many metal materials, corrosion mitigation is an issue of great importance; the U.S. spends a few percent of its gross national product per year to address corrosion issues [9,10]. Pure Al materials are resistive to corrosion due to the spontaneous formation of a slowly growing, thermodynamically stable Al_2O_3 scale that acts as a surface diffusion barrier to prevent further oxidation [11]. However, this is not the case for the Al-Mg alloy as Mg segregates to the material's surface. When this alloy is heated or exposed to the atmosphere, Mg preferentially oxidizes to MgO, which forms a poor barrier to further oxidation. MgO can readily be mechanically removed from the Al-Mg alloy's surface, leaving behind an enriched softer Al material [12,13]. Thus, it is crucial to understand Mg's segregation behavior in Al-Mg alloyed surfaces and whether segregation tendency varies with temperature, Mg concentration, and surface termination [14,15].

To date, the design of oxidation-resistant alloys and coatings has been a highly empirical process, where the chosen solution is often arrived at by a basic trial-and-error approach that is not optimum (e.g., the performance of commercial alloys can vary dramatically within a specification range). First-principles density-functional theory (DFT) calculations are an attractive alternative and have the potential of providing a robust and rigorous approach for accurately predicting protective oxidation. These DFT approaches' success has enormous technical impacts on the design, tuning, and optimization of Al-Mg for various applications [6–8,16,17]. However, the computational cost of standard DFT methods has limited the investigations of alloys to simplistic models that often differ from experiments, as environmentally specific parameters, which are often excluded from these calculations [18,19]. Previous studies have relied on classical atomistic potentials that can be applied to materials under various environmental conditions to model real-world behavior [20]. The embedded-atom method (EAM) or modified EAM (MEAM) potentials are generally used to study the dynamics of Al-Mg binary systems [21–23]. These potentials are fitted to experimental data and a quantum-mechanical database of atomic forces and energies at finite temperatures. While these classical potentials have been successful for studying simple elemental systems, the design of these potentials for alloys and complex interactions is nontrivial and relies on a laborious and user-intensive process.

This work utilizes a machine learning (ML) based on deep neural networks to approach DFT accuracy but at a fraction of its computational cost, thus accelerating time to obtain tangible results [2,24–27]. The developed ML force field's success shows that these methods have the flexibility and nonlinearity necessary to describe complex potential energy surfaces [28–34]. ML potentials suffer from transferabil-

*alsaidi@pitt.edu

ity errors associated with atomic environments not included in the training, similar to traditional classical force-fields. However, in contrast to most classical potentials, ML potentials can systematically learn and improve the potential for different properties and regions of the material's phase space. In the present study, we develop a deep neural net potential (DNP) for the Al-Mg binary alloy system via the DeepPot-SE approach [35] as implemented in DEEPMD-KIT [36,37], and DEEPPOT to systematically analyze its fidelity describing a wide range of properties. We follow an adaptive iterative-learning approach to augment the training dataset to circumvent data extrapolation in regions of the phase space that are of interest and are not adequately sampled throughout the ML process. We demonstrate that our DNP describes ordered and disordered Al-Mg systems with near-DFT accuracy as we have observed in other bimetallic systems [38,39].

Further, we apply the potential to study the impact of temperature, Mg concentration, and surface termination on potential element segregation processes. Due to the complexity of various types of surfaces (e.g., grain boundaries) present in physical alloys, it is infeasible to comprehensively evaluate each surface's effect on the degree of segregation and the fracture properties with presently available methods. A simple way to gain insight into this complicated problem is to study or simulate segregation at different low-index Al alloy surfaces such as (100), (110), and (111). We compare our predicted segregation results with previously reported EAM and experimental results to further demonstrate the predictive accuracy of this DNP.

As a compliment to simulation-based analysis, thermodynamic modeling elicits a deeper understanding of first-principles physics and allows us to make surface solute concentration predictions. The classic McLean model is the foundational equation for predicting an interface's solute concentration from the bulk solute concentration and average segregation energy [40]. Fowler and Guggenheim later improved this model by considering the effects of solute-solute interactions with the interaction term, ω [41]. A negative interaction term indicates that solutes interact repulsively, and thus their segregation will be reduced in highly concentrated regions. A positive term suggests that solutes will preferentially migrate toward other, nearby solutes. Recently, Wagih and Schuh have proposed further changes to the model for grain boundary solute segregation [42]. An assumption made in the classical approaches is that the bulk solute concentration is approximate to the total solute concentration. The new approach argues that this approximation is inaccurate for nanocrystalline systems, which contain a high share of boundary positions relative to bulk positions [42]. They instead proposed a mixture rule, solved self-consistently, to obtain the solute concentration. This new model also incorporates a piecewise function to represent solute interactions, which is needed to account for the absence of interactions with few nearby solute atoms [42]. Herein, we test the precision for each evolution of the solute segregation model by fitting them to solute concentration results from our Monte Carlo and molecular-dynamics (MC/MD) simulations. In adapting the Wagih-Schuh modeling method for surface solute segregation, we show that the revised isotherm yields the best surface concentration predictions in agreement with MC/MD data.

II. COMPUTATIONAL METHODS

A. DFT calculations

The DFT database was generated using the Vienna *Ab initio* Simulation Package (VASP) [43–46], employing the Perdew-Burke-Ernzerhof exchange-correlational functional [47] to solve the Kohn-Sham equations within periodic boundary conditions. The electron-nucleus interactions are described using the projector augmented wave (PAW) method as implemented in VASP [48,49]. In the PAW representation, Al is represented with an s^2p^1 valence configuration, while Mg is represented with s^2p^0. Single-particle orbitals are expanded in plane waves generated within a cutoff of 400 eV. We use a dense gamma-centered k grid with a 0.24-Å^{-1} spacing between k points, equivalent to $8 \times 8 \times 8$ mesh for bulk Al with a conventional four-atom face-centered cubic (fcc) unit cell. To aid in the k-grid convergence, we use Methfessel-Paxton [50] of order 1 with a 0.15-eV smearing width. We terminate the electronic self-consistent loop using a 10^{-8}-eV energy-change tolerance to ensure good convergence of energies and forces.

B. DNP training database

We aim to build a DNP that can equally describe the crystalline and amorphous phases of Al-Mg alloys, we constructed a training database that includes bulk, surfaces, and amorphous phases. The total number of configurations in the database amounts to ∼250 k configurations. Most configurations (∼100 k) were obtained for the small Al-Mg ordered compounds with less than 10 atoms per unit cell after applying different distortions to the system. The total number of Al-Mg slab models was ∼30 k, primarily using (100), (111), and (110) orientations employing supercells with 20–80 atoms. The alloys' surface configurations are obtained using fcc lattice with an Al/Mg random occupancy. The database was mainly populated from *ab initio* molecular-dynamics (AIMD) trajectories within an *NVT* ensemble (fixed number of atoms, volume, and temperature) at a temperature that ranges between 100 and 1000 K. We employed a relatively large 2–4-femtosecond time step in the AIMD simulations to decrease the correlations in the configurations along the AIMD trajectory. Using the DFT database, the training dataset comprises all energies and atomic forces.

C. Al-Mg DNP model and fitting

The DNP was developed with the DeepPot-SE approach [35] using DEEPMD-KIT [36,37], as described in detail elsewhere [38,39]. We used a cutoff radius of 6.0 Å for neighbor searching with 2.0 Å as the smooth cutoff. The maximum number of neighbors within the cutoff radius was set at 180 though a smaller value of ∼120 yielded similar accuracy potentials. The dimensions of the embedding and fitting nets are set at $25 \times 50 \times 100$ and $120 \times 120 \times 120$, respectively. The neural net is trained using Adam stochastic gradient descent method with a learning rate that decreases exponentially from

the starting value of 0.00; see Supplemental Material (SM) for further detail [51]. The input data are split into training and testing sets where the testing data are not used for optimizing the weights of the network but rather employed as an independent test for cross validation.

D. Validation of Al-Mg DNP

The validation of the Al-Mg DNP potential is described below for selected figures of merit and, in greater detail, in the SM with comparisons to literature [21–23,27,52–65] values. We utilized the Large-scale Atomic/Molecular Massively Parallel Simulator (LAMMPS, 16 Mar 2018 version) [66] for all of our atomic calculations with the DNP and initial structures were created with ATOMSK [67] unless otherwise noted. Vacancy mobility energy barriers were determined using the nudged elastic band method [68].

E. Bulk crystal lattice constant and atomic energy

Before investigating defects, optimized lattice constants and cohesive energy (E_{coh}) are determined for the bulk crystal models. For elemental Al and Mg systems, we computed the cohesive energy per atom using $E_{\text{coh}} = E_{\text{B}} - E_{\text{atom}}$, where E_{B} is the bulk energy per atom and E_{atom} is the energy of the corresponding isolated atom. Thus, with this definition, a negative E_{coh} indicates that the system is thermodynamically stable.

F. Elastic constants

In the DFT and the atomistic calculations, the elastic constants are calculated by performing 12 distortions of the lattice and then fully relaxing the system's atomic coordinates. The elastic constants are then computed using strain-stress relationships. The bulk moduli (e.g., bulk, shear, Young's moduli, and Poisson's ratios) are computed using the crystal lattice specific equations detailed in the SM [51].

G. Surface energies and planar defects

The free-surface formation energy, γs, is computed using $\gamma\text{s} = (E - NE_{\text{B}})/(2\text{A})$, where E is the energy of the slab model, and A is the surface area perpendicular to the slab direction. The factor of 2 is included to account for the two different surfaces in the slab models. We calculated Al surface energy for all terminated surfaces with Miller indices less than 4. The same approach was used for the planar defects; however, we used the DFT optimized structures from the material project database (MPDB), and compared them to the surface energies listed for these calculations.

H. Molecular-dynamics simulations

The molecular-dynamics simulations are carried out using LAMMPS [66]. First, models starting from initial ideal fcc structures are equilibrated in the *NPT* ensemble (fixed number of atoms, pressure, and temperature) to allow the volume to change to minimize the pressure at a given temperature. After this equilibration, the lattice and lattice constants are fixed, and we carried simulations in the *NVT* ensemble for data collection (100 ps). We employed a 1-fs time step in all simulations. For the alloys, we attempted a Monte Carlo (MC) swap between Al and Mg at random sites every 20 MD steps, after which the swap is accepted with a Metropolis probability. In total 400 k MD steps were run. The bulk systems are represented using an $8 \times 8 \times 8$ supercell of the conventional unit cell corresponding to 2048 atoms with periodic boundary conditions. The surface models are constructed using a 6×6 surface supercell for the (100) and (110) surfaces and a 6×5 supercell for the (111) terminations. The number of layers in the slab models is 80, 64, and 96 for the (100), (110), and (111) slabs, resulting in 2880 atoms for (100) and (111) slabs and 2304 for the (110) slab.

TABLE I. Comparison of general bulk properties of Al.

Property	Experiment	DNP	DFT
fcc a	4.05 [53]	4.04	4.04
fcc E_{coh}	−3.49 [54]	−3.75	−3.655 [27]
V_0	16.5 [55]	16.51	16.47
C_{11}	114.3 [60]	118	104
C_{12}	61.9 [60]	65	73
C_{44}	31.6 [60]	38	32
Bulk modulus (K_H)	79.4 [60]	82	83
Shear modulus (G_H)	29.4 [60]	33	24
Young's modulus (E_H)	78.51 [60]	88	68[a]
Poisson's ratio (υ)	0.33 [61]	0.32	0.37

All DFT values are from MPDB [52], mp-131 unless otherwise noted. Lattice parameters are in Å, V_0 in Å^3/atom, C_{xx} and elastic moduli in GPa.
[a]Calculated from literature reference values.

III. RESULTS AND DISCUSSION

We report the results of iteratively training Al-Mg DNP model, the DNP accuracy reproducing bulk Al and Mg figures of merit relative to DFT and description/comparison of Al-Mg surface segregation dynamics with DFT and experimental reference values. The description and quantified accuracy of the DNP predictions, with reference DFT values, establish the general utility, flexibility and versatility of this DNP for use in modeling Al-Mg, Al or Mg materials in future works.

A. Force-field validation

The Al-Mg DNP was validated by comparing to commonly known physical properties based on our calculations using DFT or obtained from the literature. For each metal, we compared our DNP calculated values for lattice parameter and cohesive energy (face-centered cubic, body-center cubic, simple cubic, diamond, hexagonal close-packed), point defects (vacancies and interstitial atoms), elastic constants (bulk modulus, Young's modulus, shear modulus, and Poisson's ratio), surface energy, to list a few in Tables I and II (see Tables SI and SII for entire list [51]). The DFT calculations are carried out using an equivalent computational setup as employed to generate the training dataset.

The general bulk properties of Al and Mg agree well with the values found in MPDB [52] in addition to the elastic constants (see SM [51] for more details). We also observe good

TABLE II. Comparison of general bulk properties of Mg.

Properties	Experiment	DNP	DFT
a_{hcp}	3.209 [69]	3.18	3.203
c_{hcp}	5.211 [69]	5.25	5.127
hcp E_{coh}	−1.51 [62]	−1.50	−1.49 [27]
V_0	23.24 [63]	23.05	23.04
C_{11}	63.5 [65]	78	58
C_{12}	25.9 [65]	28	30
C_{13}	21.7 [65]	20	22
C_{33}	66.5 [65]	74	66
C_{44}	18.4 [65]	15	20
C_{66}	18.8 [65]	22	14
Kv	36.9 [65]	41	37
K_R		36	37
Bulk modulus (K_H)		38	37
Young's modulus (E_H)	45 [65]	51	46[a]
G_V	19.4 [65]	21	18
G_R		19	17
Shear modulus (G_H)		20	18
Poisson's ratio (v)	0.295 [61]	0.28	0.29

All DFT values are from the MPDB [52], mp-153 unless otherwise noted. Lattice parameters are in Å, E_0 in eV, V_0 in Å^3/atom, C_{xx} and elastic moduli in GPa.

[a]Calculated from literature reference values.

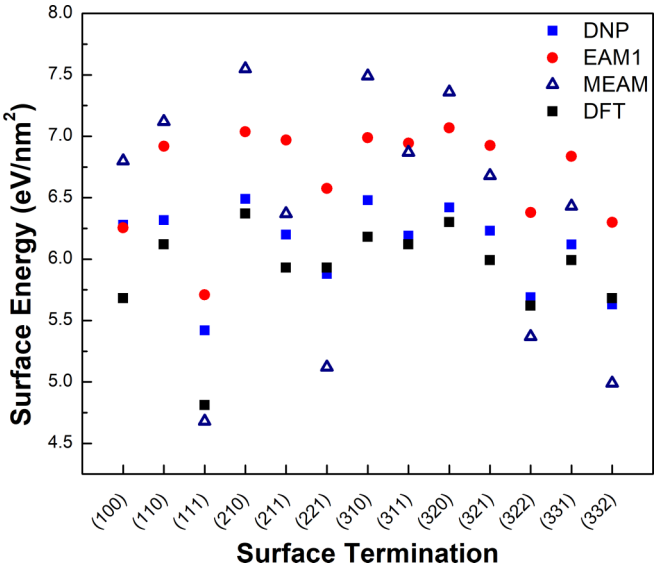

FIG. 1. Al surface energies (eV/nm^2) for terminations with Miller indices <4 computed using optimized DFT structures (MPDB, mp-131) with DNP, EAM1, and MEAM literature values [27].

agreement with experimentally measured values in Tables I and II for Al and Mg with the DNP and literature DFT values. Further, the high-fidelity reproduction of the elastic constants and associated moduli is a good indication of a potential's accuracy [70]. We note that some of the DNP mechanical properties are over- or underestimations of the DFT literature values. These differences between the DNP and DFT results are likely due to differences in the computational setup employed by MPDB and in generating DNP training set (e.g., energy cutoff energies 520 and 400 eV, respectively). In addition, these differences could be in part due to inaccuracies of the DNP. Similar over and underestimations in these values are noted when comparing the EAM and MEAM potentials (see Tables SI and SII [51]).

B. Surface energies and planar defects

We used optimized DFT structures from the MPDB and their reported surface energies for comparison with DNP, EAM1 [23], EAM2 [21], EAM3 [22], and literature values [27] from a MEAM [71] potential. The calculated EAM2 and EAM3 surface energies are reported in Table S1 but were excluded from Fig. 1 due to their poor accuracy compared to DFT reference values. Comparison of the surface energies for terminated Al surfaces with Miller indices less than 4 are in excellent agreement [<6% energy difference, using Eqs. (S1) and (S2) with DFT values [51]] (Fig. 1 and Table SI). In addition to the idealized surfaces listed in Fig. 1 and Table SI, we also investigated a small set of grain boundaries defects that are commonly found in real-world materials.

Although we did not explicitly include these planar defect structures in the training dataset, the DNP predicts the expected DFT energies of these defects relatively well (Table III). We observe satisfactory agreement of the DNP with our DFT calculations for Al planar defects structures and the surfaces (Fig. 1 and Table III). We note that this current version of the DNP fails to accurately describe the Σ7(111) planar defect energy (∼75.4% difference) compared to DFT values. Nevertheless, the DNP's accuracy is remarkable at reproducing DFT values not included in the training set.

C. Al-Mg DNP validation summary

Detailed descriptions of these bulk property calculations and corresponding DFT values can be found in the SM [51], a total of 46 properties for Al and Mg, respectively (Tables SI and SII, and Fig. S1). In general, our DNP agrees well with DFT values (%E_{DIFF}) by 8.12, 14.8, and 11.2% for all Al, all Mg, and all Al and Mg, respectively (see SM [51] for details). We compared these benchmark properties to values calculated using three well-described Al-Mg EAMs [21–23] and literature values calculated with MEAM style [27] poten-

TABLE III. Comparison of DNP bulk Al planar defects surfaces energies (eV/nm^2) with DFT. N.B., this class of structures were not included in DNP training.

Sigma	Defect plane	Rotation plane	Rotation	γ_s Al DNP	γ_s Al DFT [52]	% E_{Diff}
3	$(1\bar{1}\bar{1})$	(110)	180.0	206	193	6.45
5	$(0\bar{1}\bar{3})$	(100)	53.13	310	300	3.33
5	$(0\bar{2}\bar{1})$	(100)	36.87	345	331	4.34
5	(100)	(100)	36.87	213	237	10.3
7	(111)	(111)	36.87	142	811	75.4
7	$(3\bar{2}\bar{1})$	(111)	38.21	322	312	3.20
9	(110)	(110)	38.94	427	443	3.66
9	$(2\bar{2}\bar{1})$	(110)	38.94	285	268	6.05

All DFT values are taken from the MPDB mp-131 dataset.

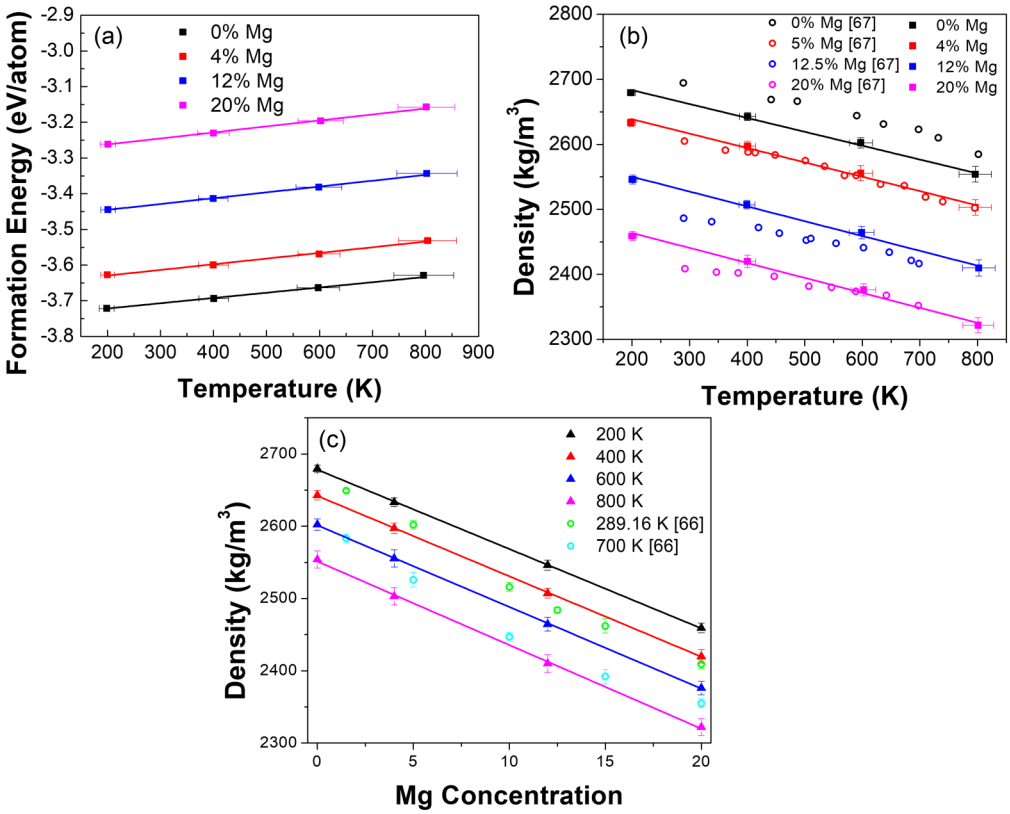

FIG. 2. Bulk properties of the Al-Mg (Mg = 0, 4, 12, and 20%) alloy from DNP: (a) formation energy as a function of temperature; (b) density as a function of temperature (200 to 800 K); (c) density as a function of Mg concentration. Error bars indicate twice the standard deviation (2σ).

tials. Overall of the examined properties, our DNP potential is more accurate than the EAM/MEAMs at reproducing the literature DFT results. This observation is not surprising as the EAM/MEAM potentials generally are optimized using both DFT structures and experimentally determined figures of merit, which results in a deviation from DFT-only calculations. Additionally, EAMs generally do not have good accuracy outside of their training sets [72].

D. Bulk properties of Al-Mg alloy system

Before investigating Mg surface segregation, we calculated the formation energy of the Al-Mg alloy (Mg = 0, 4, 12, and 20% atomic ratio) and its density as a function of temperature (K) using a hybrid Monte Carlo/molecular dynamics scheme via LAMMPS software package (Fig. 2). Mg's cohesive energy is smaller than Al (see Tables I and II), which explains the decrease in the formation of the energy of Al-Mg with increasing Mg concentration. The slope of the fitted lines increases nonlinearly for 0, 4, 12, and 20% Mg at 0.33 ± 0.2, 0.33 ± 0.2, 0.35 ± 0.2, and 0.36 ± 0.2 eV/K, respectively. This observation could be related to physical phenomena such as reducing the alloy melting point [73]. Additionally, we observe a linear trend [Fig. 2(b), adjusted $R^2 > 0.991$] [74] in the Al-Mg density as a function of temperature [Fig. 2(b)] and also atomic Mg% [Fig. 2(c)], both observations have negative slopes, a trend which is consistent with the experimental literature [74,75]. The alloy's density and its formation energy are also observed to decrease linearly (adjusted $R^2 > 0.998$) as a function of %Mg for all the temperatures simulated [Figs. 2(b) and 2(c)], which are also consistent with experimental observations in the literature [74,76].

E. Surface segregation

The heat of segregation at $T = 0$ K for Mg impurities in Al slabs is shown in Fig. 3. The segregation energy is defined as the energy difference between placing an impurity atom in the bulklike layers away from the surface versus top surface layers. Here the lattice is fixed as in the bulk configuration. We have investigated surface segregation for all distinct surfaces with a Miller index no larger than 3. Solute substitution at the top layer is the most favorable for all surfaces, indicating Mg's tendency to segregate to the top layers. For example, Mg is favorable to substitute Al on the top layer by ~0.4 eV compared to that in a "bulklike" environment away from the surface. Among the low-index flat surfaces, (111) surface has the weakest segregation tendency though the energy difference is not significant. We find that Mg segregation prefers step edge for stepped surfaces while the terrace sites also show segregation tendency. However, regardless of the surface termination, the DFT results suggest that Mg segregates to the surface. The surface segregation tendency depends on several factors, including atomic size, cohesive energy, and surface energy [77]. Mg atomic size is ~12% larger than that of Al atom, and its cohesive energy is 60% smaller than that of Al.

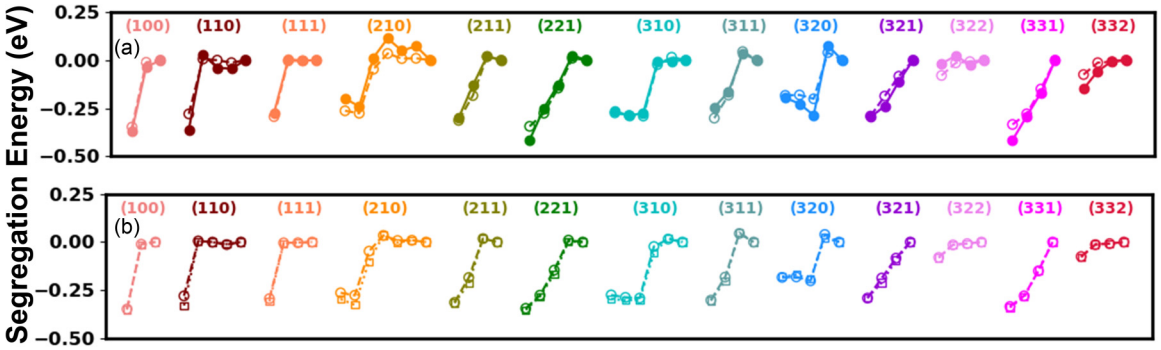

FIG. 3. Mg heat of segregation at 0 K (eV/atom) for Al surfaces with Miller indices no larger than 3. The solute's energies are shown to occupy layers of increasing depth from the surface from left to right for each surface. (a) Comparison between DFT filled circles/solid line and DNP open circles/dashed line using 2 × 2 surface supercells. (b) Comparison between DNP with 2 × 2 (open) circles, dashed/line and 8 × 8 (open) squares, dashed line, surface supercells. Lines are added to guide the eye.

As a result, Mg prefers to segregate to the top surface layers. From geometrical inspection of the optimized structures, the larger Mg atoms are accommodated on the top surface layers by moving ∼0.3 Å along the z axis, while Mg atom from the subsurface or subsubsurface layers shows a smaller ∼0.1-Å outward movement.

Figure 3(a) compares the DFT segregation energies with the DNP results on the same surface models. As seen from the figure, we have an excellent agreement between DFT and DNP results. Because of the high computational cost of DFT simulations for large systems, all surface calculations in Fig. 3(a) are done using a relatively small 2 × 2 surface supercell (see Table SIII [51]). We carried out additional calculations using an 8 × 8 surface supercell utilizing our DNP to investigate the impact of finite-size effects. Figure 3(b) shows an excellent agreement between the small and larger supercells suggesting relatively small finite-size effects. Our results compare well previous results by Liu *et al.*, who reported energies of the Mg heat of segregation [21]. While Deng *et al.* modified analytic EAM (MAEAM) potential [78] observes a similar trend in heats of Mg segregation energies, the reported values are significantly different for all terminations. Both Liu *et al.* and our DNP are similar to the experimentally calculated value of −0.21 eV for the (111) plane [79]. The values are distinct for predictions of Mg heat of segregation energy for (100) and (110) terminations due to these potentials' assumptions and training parameters. Our DNP and DFT Mg surface segregation enthalpy results are consistent with each other and distinct from these EAM potentials.

We have carried out hybrid MC/MD simulations based on energies and forces computed using the DNP to investigate the segregation at finite temperature and higher Mg substitutions. This scheme involves short molecular-dynamics runs and random exchange between atoms at different locations, in which the last configuration is accepted or rejected using a standard Metropolis algorithm. MC/MD is advantageous as it automatically accounts for impurity-impurity or impurity-host interactions, temperature, configurational entropy, and atomic vibrations. Using the optimized lattice constants determined before, from the *NPT* simulations, we constructed slab models for the (100), (110), and (111) surfaces with thicknesses of 80, 64, and 96 layers, respectively. Following MC/MD simulations, we obtained the slabs' equilibrium structures at various temperatures and Mg compositions.

As the simulation temperature is increased from 200 to 800 K, we observe decreased Mg concentrations at the top layers, as seen in Fig. 4 and Fig. 5. Mg surface segregation is observed to be the largest for (110) surfaces, for all temperatures and Mg compositions, and at temperatures below 800 K [Figs. 4(a), 4(b), and 4(c)]. Comparatively, surface segregation tendency is weakest for the (111) termination across all temperatures and Mg compositions [Fig. 4(c)]. In good agreement with literature reports obtained using EAM2 [21], the termination-dependent segregation tendency follows the ordering: (111)<(100)<(110) [Figs. 4(a) and 4(b)]. We also observe expected decreases in Mg surface enrichment as the temperature increases from 200 to 800 K for all surfaces [Fig. 4(d)], with (111) and (100) showing the lowest and highest Mg enrichment, respectively. Lastly, the surface enrichment results show that a significant proportion of solute atoms are in the surface layer at low total Mg compositions and low temperatures.

As expected, we observe a more significant mixing of Al and Mg in the slab's interior as temperature increases, and an increase in the interior Mg concentration occurs (Fig. S2 [51]). We also observe that Mg segregation is restricted to the 4–5 topmost layers. Mg concentration in these subsurface layers increases linearly with increasing temperature relative to the interior, as is observed in the surface layers at each composition 4, 12, and 20% of all terminations (Fig. S3 [51]). Analysis of the slopes of these fitted lines from Fig. S3 displays the overall changes in the interior Mg concentration of the Al-Mg slabs (Mg = 4, 12, 20%) surface termination dependent with the largest change observed in the order of (100)>(110)>(111) (Fig. S4 [51]). These observations, of the interior Mg concentration, further support that there is less of a driving force for Mg segregation in the (111) terminated slab as temperature and Mg concentration change, e.g., internal Mg concentrations remain relatively high compared to (100) and (110) slabs. Interestingly, regardless of the Al-Mg slab % Mg concentration, the concentrations of the Mg surface (and subsurface) remain relatively consistent for each temperature for a given termination (Fig. 5 and Fig. S3). To directly compare with Liu *et al.* (4% composition) results, we looked at the ratio of surface % Mg to the interior [Fig. 4(d)]. We

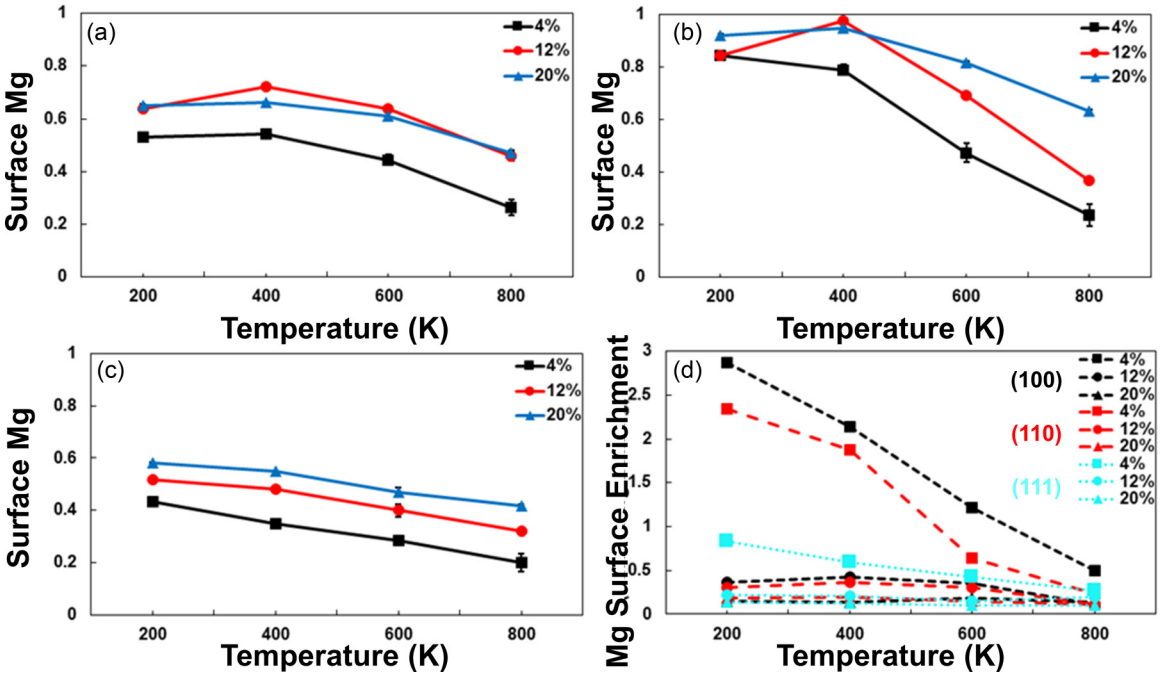

FIG. 4. Mg concentration in the surface layer computed using MC/MD simulations with the DNP at $T = 200, 400, 600, 800$ K for (a) (100), (b) (110), and (c) (111) surfaces, and (d) Mg surface enrichment relative to the bulk (black/dots = (100), red/dashed (110), and cyan/dots = (111)). Error bars indicate the standard deviation (σ).

observe good agreement with Liu *et al.* for the (100) termination, but weaker agreement in the ratio is observed for the (111) termination. We also note that for the (110) termination, the subsurface (second layer) Mg concentration approaches surface concentration at 800 K for all Al-Mg slabs examined.

Ideally, a further quantitative comparison to experimental results would support our computational models; however, this comparison is difficult because of experimental parameters that inhibit comparison at elevated temperatures. Auger electron spectroscopy (AES) investigations provide an excellent method for Mg surface segregations examination as the Auger electrons have lower penetration depth in a material compared to x-ray photoelectron spectroscopy. An AES study of Al-0.88at%Mg alloy found a surface enrichment of Mg about 10.5 at. % at 473 K [80]. Bloch *et al.* also found Mg's surface segregation for Al-1.45 at. %Mg alloys using optical second-harmonic generation, and Mg was observed to decrease beyond 510 K due to evaporation [81]. The Mg's evaporation is favorable under the ultrahigh-vacuum ($<1 \times 10^{-9}$ Torr) conditions required for AES; however, Mg evaporation is not included in our MC/MD models. Therefore, we do not expect to see consistent agreement between these types of high-temperature experimental data for Mg surface concentration.

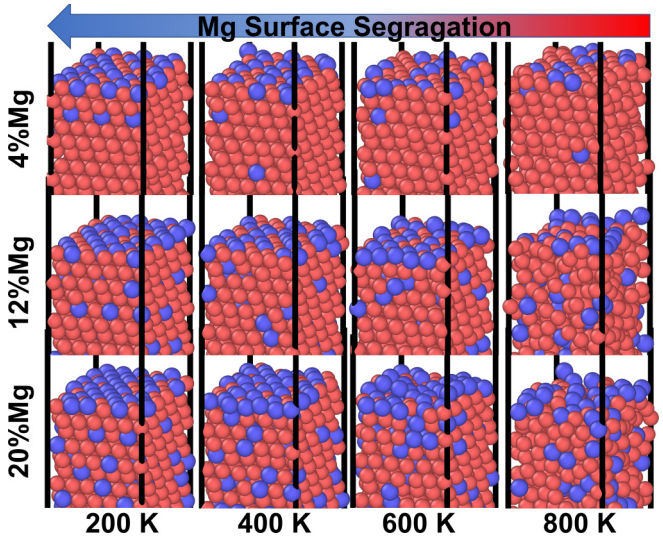

FIG. 5. Geometrical structures of Al-Mg alloy (111) surface with different Mg ratios (Mg = 4, 12, and 20%) at 200, 400, 600, and 800 K using MC/MD and the DNP. The blue circles are Mg, and the red circles are Al.

Nevertheless, these experimental challenges at elevated temperatures highlight the importance of theoretical models that can elucidate the temperature-dependent dynamics of Al-Mg alloys (and other materials); see Fig. 4. The fraction of Mg (Fig. S2) suggests that Al-Mg alloys with (111) exposed surfaces (visualized in Fig. 4) are ideal for corrosion resistance as these have the weakest tendency to segregate Mg to the surface and lower potential of Mg loss via oxidation to MgO [23]. A similar observation of the (111) Al-Mg surface using a MAEAM potential was reported by Deng *et al.* [78]. Therefore, we suggest that our hybrid MC/MD approach is qualitatively consistent with the experimental results.

Figure 6 shows the pair distribution function (PDF) for the three alloy surfaces with 4% Mg doping concentration at three different temperatures ($T = 400, 600$, and 800 K). The PDF $g(r) = \langle \sum_i \sum_{j \neq i} \delta(r - r_{ij}) \rangle_{\mathrm{MC/MD}}$ is obtained from the ensemble average of the configurations generated using the MC/MD approach. As seen from the figure, the Al-Al,

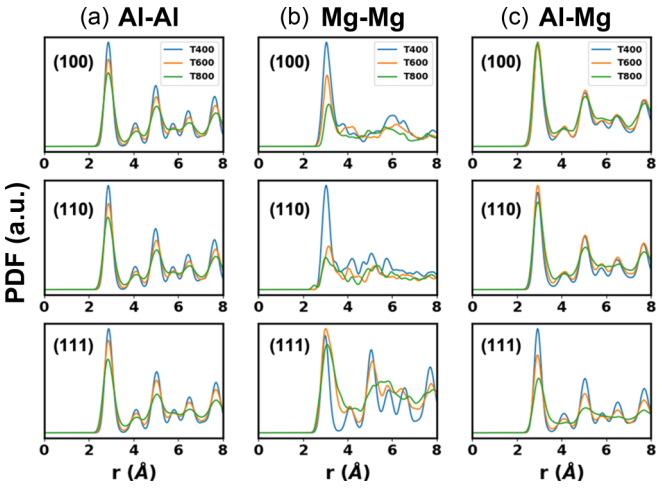

FIG. 6. The ensemble-averaged radial distribution function for (a) Al-Al, (b) Mg-Mg, and (c) Al-Mg for the Al-4%Mg alloy surfaces at three different temperatures and the three different surfaces using MC/MD and the DNP.

Mg-Mg, and Al-Mg PDFs show a dominant first peak at $r \sim 2.85$, 3.1, and 2.9 Å, respectively, which is consistent with the nearest-neighbor distance in the fcc lattice. The larger values for Mg-Mg and Al-Mg are consistent with Mg's larger ionic size compared to Al. As shown in Fig. 4, at low temperatures, Mg atoms mostly occupy the top surface layer. The Al-Mg increased intensity compared to Mg-Mg indicates that Mg is likely coordinated with Al (not Mg). Indeed, we have verified based on DFT calculations that two Mg atoms do not prefer to be nearest neighbors, likely because of the increase in the misfit strain. Expectantly, the temperature has a smoothening effect on the peaks that are most noted for the open (110) surface for Mg-Mg. The reduction of the peak intensities and boarding concerning temperature indicates a transition from the crystalline fcc state to a more disordered and likely a liquid state [82]. Of all Al-Mg interactions, the (100) surface is the least impacted by temperature, presumably because most Mg has migrated to the surface, segregated, and the phase change is small.

The MC/MD surface segregation results are also valuable in developing a new thermodynamic model, which may provide superior predictions of the surface solute concentration over the standard literature methods. The traditional isotherm used to describe solute segregation, developed by McLean, utilizes statistical mechanics to relate the atomic fraction of solutes in a system's bulk and interface regions [40]. This method for obtaining solute concentrations postrelaxation is applicable to surface interfaces, as presented in Eq. (1):

$$\frac{X_{\text{surf}}}{1 - X_{\text{surf}}} = \frac{X_{\text{bulk}}}{1 - X_{\text{bulk}}} \exp\left(-\frac{\Delta \bar{E}_{\text{seg}}}{kT}\right). \tag{1}$$

The surface segregation concentration, X_{surf}, is described as a function of the bulk solute concentration, X_{bulk}, Boltzmann's constant, k, and temperature, T. The isotherm incorporates an average segregation energy term, $\Delta \bar{E}_{\text{seg}}$, which is the energy difference between a single solute atom in the surface layer and a bulk layered solute atom. The segregation energy is highly dependent on the configurational energy and elastic strain energy changes during atom exchange [83]. A fundamental assumption made by McLean is that the total solute concentration of the system, X_{tot}, is equal to X_{bulk}, allowing one to produce X_{surf} from X_{tot}.

Fowler and Guggenheim [41] later adapted the McLean isotherm to account for the interaction between segregating solutes by adding a solute-solute interaction term ω. As solutes continue to segregate to the surface layers of a system, the energetic attraction or repulsion between them increases. In Al-Mg alloy, we verified that the segregation tendency declines in the case of a repulsive solute interaction. Adding the solute interaction term to the McLean isotherm, we arrive at Eq. (2):

$$\frac{X_{\text{surf}}}{1 - X_{\text{surf}}} = \frac{X_{\text{bulk}}}{1 - X_{\text{bulk}}} \exp\left(-\frac{\Delta \bar{E}_{\text{seg}} + \omega \cdot X_{\text{surf}}}{kT}\right). \tag{2}$$

Most recently, novel additions to the McLean-Fowler-Guggenheim model were proposed by Wagih and Schuh [42] for grain boundary segregation. In this model, the improvements to the Fowler-Guggenheim isotherm are seen in its superior ability to extend a single set of fitted parameters to a wide temperature and composition space. Although the Wagih-Schuh study is focused at decoupling the effects of grain boundary site spectrality from the model, their other innovations can be applied to surface solute segregation as well. Namely, relevant to our study are their suggestions to cast the Fowler-Guggenheim isotherm with a mixture rule and represent the solute interaction as a piecewise energy term, ΔE^{ω}, dependent on the dilute limit of the system.

The mixture rule consideration is needed as a system with a low total solute concentration contains a significantly large proportion of solutes located within its surface layers after segregation. As a result, the earlier models' approximation, $X_{\text{tot}} = X_{\text{bulk}}$, is incorrect, and a substitution of the X_{surf}, utilizing the surface site fraction, f, or ratio surface lattice positions to total lattice positions, should be applied. Our experimental results presented in Fig. 4(d) show that the low-temperature, 4% total Mg systems, contain significantly higher proportions of solutes in the surface layers than in the bulk, confirming this step's physical necessity. Poor predictions in the low total solute concentration region arise in the absence of this correction. Thus, we substitute out X_{surf} in Eq. (2) using the mixture rule, Eq. (3), and rewrite, resulting in Eq. (4).

$$X_{\text{tot}} = (1 - f_{\text{surf}}) X_{\text{bulk}} + f_{\text{surf}} X_{\text{surf}}, \tag{3}$$

$$X_{\text{tot}} = (1 - f_{\text{surf}}) X_{\text{bulk}} + f_{\text{surf}} \left[1 + \frac{1 - X_{\text{bulk}}}{X_{\text{bulk}}} \exp\left(\frac{\Delta \bar{E}_{\text{seg}} + \Delta E^{\omega}}{kT}\right)\right]^{-1}. \tag{4}$$

Equation (4) is solved self-consistently to determine X_{bulk} from X_{tot}, which simultaneously solves X_{surf} via Eq. (3). The segregation energy, $\Delta \bar{E}_{\text{seg}}$, and solute interaction energy, ΔE^{ω}, are determined by fitting the equations to experimental results.

Further, adopting the Wagih-Schuh approach for surfaces is accomplished by evaluating the solute interaction energy as a piecewise function. As presented in Eq. (5), the interaction energy is 0 below the dilute limit, and a linear function above it, which is necessary as the solute interaction energy

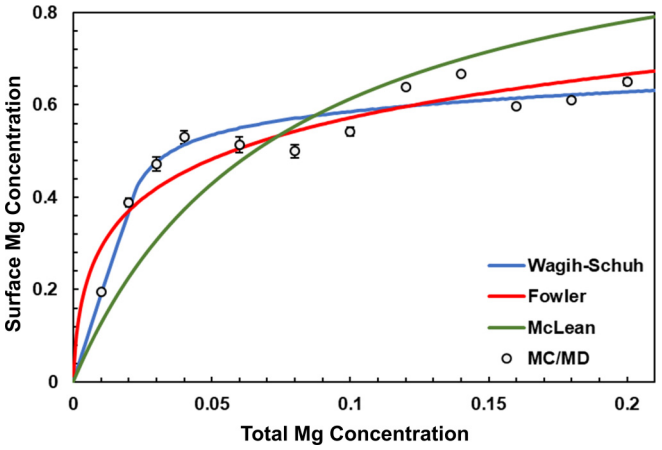

FIG. 7. MC/MD simulation data and fitted predictions of the McLean [Eq. (1)] [40], Fowler-Guggenheim [Eq. (2)] [41], and Wagih-Schuh [Eqs. (3), (4), and (5)] [42] models for the (100) surface at 200 K. Error bars indicate the standard deviation (σ).

is negligible at low total concentrations ($<10\%\, X_{\text{surf}}$) due to neighboring solute atoms being too distant to interact given the interatomic potential [42]

$$\Delta E^{\omega}(X_{\text{surf}}) = \begin{cases} 0 & X_{\text{surf}} \leqslant X_0 \\ \omega(X_{\text{surf}} - X_0) & X_{\text{surf}} > X_0 \end{cases}. \tag{5}$$

The surface-adapted Wagih-Schuh model shows a significant improvement in its predictive capabilities over the Fowler-Guggenheim and McLean models. Average prediction errors, or the mean of differences between MC/MD data points and fitted isotherm predictions, are reduced, especially around the low total solute concentration region ($\leqslant$2% Mg). Figure 7 displays one such fitting of each isotherm for the (100) surface at 200 K, in which the Wagih-Schuh model's prediction error is 50% that of the Fowler-Guggenheim model and 33.3% of the McLean model, Fig. 8.

The average prediction errors for the entire temperature and surface termination space are presented in Fig. 8. Overall, the Wagih-Schuh model displays the lowest errors, with the most noticeable differences in the (100) surface termination. The improved predictive capabilities are attributed to the piecewise function accounting for the low concentration region where solutes do not interact, as instead, solutes separate beyond their interaction distance. The mixture rule casting of the Fowler-Guggenheim model also enables a better representation of the low surface concentration region since most solute atoms are in the surface layer. Full parameter fitting results from each isotherm are found in Table SIV [51].

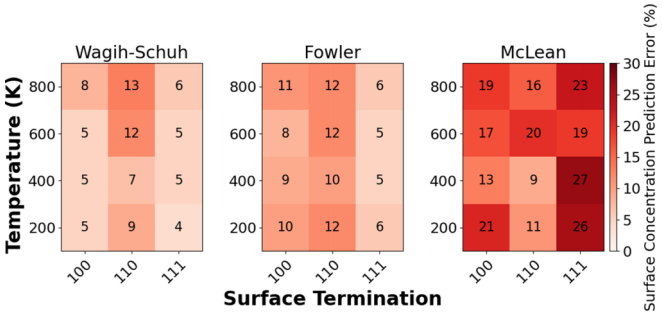

FIG. 8. Average prediction errors of each model with simulation results. The difference between each model's fitted curves and actual simulation points is averaged along with the entire composition range. The errors for each temperature and surface termination combination are labeled according to the colormap bar on the right.

Consistent with our simulation results, the isotherm predictions of the (111) surface show the lowest concentrations and segregation energies. A possible explanation is that the higher packing density of (111) improves the likelihood that neighboring solute atoms fall within the interatomic potential's interaction distance. A shorter average separation between solutes increases the likelihood that each solute atom will interact with more than one neighboring solute [42]. Given that the interaction's nature is repulsive, this limits solute migration to the highly concentrated surface. The radial distributions shown in Fig. 6 support this correlation; the (111) surface contains the largest variance of solute pair radii and the largest solute separation. Additionally, the close packing of (111) may enhance the misfit strain between paired solutes, spreading energetically favorable surface positions. It remains unclear the relation between the dilute limit of the system and the surface termination. A variable dilute limit would affect the piecewise solute interaction energy term in determining which concentration solute interactions begin. Further testing of the thermodynamic model is needed to determine the dilute limit's physical nature, enabling more efficient parameter fitting.

IV. CONCLUSIONS

We have developed a robust atomistic potential based on machine learning principles using the DeepPot-SE approach. Our DNP was validated against DFT values in the literature or calculated by us, confirming that that the developed Al-Mg DNP has high fidelity for calculating Al and Mg's general bulk properties. Furthermore, our DNP can reproduce DFT benchmarks for volume, density, and Al-Mg alloy systems' formation energy using a MC/MD approach. Additionally, we can accurately model Mg surface segregation behavior in larger simulation cells ($8 \times 8 \times 8$) while maintaining DFT accuracy. Our results suggest that the (111) surface is ideal for optimal corrosion resistance as Mg segregation is the lowest compared to the (100) and (110) surfaces. Surprisingly, careful selection of the Al-Mg alloy's Mg composition also impacts the surface segregation where 12–20% total Mg concentration shows the weakest segregation at the surface and a more uniform Mg distribution throughout. A thermodynamic model of Mg surface segregation in Al-Mg systems was developed, by adapting the isotherm by Wagih-Schuh to accurately predict surface solute concentrations in coordination with these results, which was achieved by eliminating the bulk solute approximation made in earlier models and incorporating a piecewise solute interaction energy term. The thermodynamic model's predictions also support the (111) surface having the lowest surface segregation energy of all studied terminations, which is explained by the higher packing density of (111), causing a smaller average separation between solute atoms and thus an increased misfit strain which spreads apart

energetically favorable surface positions. Future work is needed to mathematically describe the termination dependency of the dilute limit to enable faster parameter fitting of the isotherm. This work will help accelerate the selection and real-world testing of Al-Mg alloys that are more resistant to corrosion by serving as the basis for developing of DNP to evaluate the addition of dopants, such as beryllium [84].

The training database and the potential are freely available [85].

ACKNOWLEDGMENTS

We are grateful for the U.S. National Science Foundation Award No. CSSI-2003808. Also, we are grateful for computing time provided in part by the Pittsburgh Center for Research Computing (CRC) resources at the University of Pittsburgh and Argonne Leadership Computing Facility, a DOE Office Science User Facility supported under Contract No. DE-AC02-06CH11357.

[1] W. F. McDonough and S.-S. Sun, Chem. Geol. **120**, 223 (1995).
[2] Y. Liu, C. Niu, Z. Wang, Y. Gan, Y. Zhu, S. Sun, and T. Shen, J. Mater. Sci. Technol. **57**, 113 (2020).
[3] A. A. Luo, E. A. Nyberg, K. Sadayappan, and W. Shi, in *Essential Readings in Magnesium Technology*, edited by S. N. Mathaudhu *et al.* (Springer International Publishing, Cham, 2016), pp. 41.
[4] H. Friedrich and S. Schumann, J. Mater. Process. Technol. **117**, 276 (2001).
[5] X. J. Wang, D. K. Xu, R. Z. Wu, X. B. Chen, Q. M. Peng, L. Jin, Y. C. Xin, Z. Q. Zhang, Y. Liu, X. H. Chen, G. Chen, K. K. Deng, and H. Y. Wang, J. Mater. Sci. Technol. **34**, 245 (2018).
[6] N. Winzer, A. Atrens, G. Song, E. Ghali, W. Dietzel, K. U. Kainer, N. Hort, and C. Blawert, Adv. Eng. Mater. **7**, 659 (2005).
[7] S. Toros, F. Ozturk, and I. Kacar, J. Mater. Process. Technol. **207**, 1 (2008).
[8] S. You, Y. Huang, K. U. Kainer, and N. Hort, J. Magnes. Alloy. **5**, 239 (2017).
[9] G. H. Koch, M. P. H. Brongers, N. G. Thompson, Y. P. Virmani, and J. H. Payer, *Corrosion Cost and Preventive Strategies in the US* (NACE International, Houston, TX, 2001).
[10] R. E. Ricker, Science **252**, 1232 (1991).
[11] H. Liu, F. Cao, G.-L. Song, D. Zheng, Z. Shi, M. S. Dargusch, and A. Atrens, J. Mater. Sci. Technol. **35**, 2003 (2019).
[12] E. Ghali, W. Dietzel, and K.-U. Kainer, J. Mater. Eng. Perform. **13**, 7 (2004).
[13] N. Mo, Q. Tan, M. Bermingham, Y. Huang, H. Dieringa, N. Hort, and M.-X. Zhang, Mater. Des. **155**, 422 (2018).
[14] G. K. Sigworth, *Best Practices in Aluminum Metalcasting* (American Foundry Society, Schaumburg, IL, 2014).
[15] R. Bruce, L. Ingerman, and A. Jarabek (Environmental Protection Agency, Washington, DC, 1998), https://cfpub.epa.gov/si/si_public_file_download.cfm?p_download_id=473360.
[16] R.-c. Zeng, J. Zhang, W.-j. Huang, W. Dietzel, K. U. Kainer, C. Blawert, and W. Ke, Trans. Nonferrous Met. Soc. **16**, s763 (2006).
[17] H. Hornberger, S. Virtanen, and A. R. Boccaccini, Acta. Biomater. **8**, 2442 (2012).
[18] C. Nyshadham, M. Rupp, B. Bekker, A. V. Shapeev, T. Mueller, C. W. Rosenbrock, G. Csányi, D. W. Wingate, and G. L. W. Hart, Npj Comput. Mater. **5**, 51 (2019).
[19] G. P. P. Pun, R. Batra, R. Ramprasad, and Y. Mishin, Nat. Commun. **10**, 2339 (2019).
[20] A. Vaida, J. Guénoléb, A. Prakash, S. Korte-Kerzelb, and E. Bitzeka, Materialia **7**, 100355 (2019).
[21] X.-Y. Liu, P. Ohotnicky, J. Adams, C. L. Rohrer, and R. J. Hyland, Surf. Sci. **373**, 357 (1997).
[22] M. I. Mendelev, M. Asta, M. J. Rahman, and J. J. Hoyt, Philos. Mag. **89**, 3269 (2009).
[23] X. Y. Liu and J. B. Adams, Acta Mater. **46**, 3467 (1998).
[24] Y. Juan, Y. Dai, Y. Yang, and J. Zhang, J. Mater. Sci. Technol. **79**, 178 (2021).
[25] J. E. Gubernatis and T. Lookman, Phys. Rev. Mater. **2**, 120301 (2018).
[26] K. Choudhary, B. DeCost, and F. Tavazza, Phys. Rev. Mater. **2**, 083801 (2018).
[27] L. Zhang, D.-Y. Lin, H. Wang, R. Car, and W. E, Phys. Rev. Mater. **3**, 023804 (2019).
[28] S. Lorenz, A. Groß, and M. Scheffler, Chem. Phys. Lett. **395**, 210 (2004).
[29] B. G. Sumpter and D. W. Noid, Chem. Phys. Lett. **192**, 455 (1992).
[30] S. Manzhos, R. Dawes, and T. Carrington, Int. J. Quantum Chem. **115**, 1012 (2015).
[31] S. Manzhos and T. Carrington, Jr., J. Chem. Phys. **125**, 084109 (2006).
[32] A. P. Bartok, M. C. Payne, R. Kondor, and G. Csanyi, Phys. Rev. Lett. **104**, 136403 (2010).
[33] J. Behler and M. Parrinello, Phys. Rev. Lett. **98**, 146401 (2007).
[34] S. Chmiela, H. E. Sauceda, K. R. Muller, and A. Tkatchenko, Nat. Commun. **9**, 3887 (2018).
[35] L. Zhang, J. Han, H. Wang, W. A. Saidi, R. Car, and E. Weinan, *End-to-End Symmetry Preserving Inter-atomic Potential Energy Model for Finite and Extended Systems* (Curran Associates, Inc., Red Hook, NY, 2018), p. 4441-4451.
[36] DeePMD-Kit https://github.com/deepmodeling/deepmd-kit#the-deeppot-se-model.
[37] H. Wang, L. Zhang, J. Han, and E. Weinan, Comput. Phys. Commun. **228**, 178 (2018).
[38] C. M. Andolina, P. Williamson, and W. A. Saidi, J. Chem. Phys. **152**, 154701 (2020).
[39] C. M. Andolina, M. Bon, D. Passerone, and W. A. Saidi, J. Phys. Chem. C **125**, 17438 (2021).
[40] D. McLean, *Grain Boundaries in Metals* (Clarendon Press, Oxford, 1957).
[41] R. H. Fowler, *Statistical Dhermodynamics* (CUP Archive, Cambridge, U.K., 1939).
[42] M. Wagih and C. A. Schuh, Acta Mater. **199**, 63 (2020).
[43] G. Kresse and J. Furthmüller, Phys. Rev. B **54**, 11168 (1996).
[44] M. Shishkin, M. Marsman, and G. Kresse, Phys. Rev. Lett. **99**, 246403 (2007).

[45] G. Kresse and J. Hafner, Phys. Rev. B **47**, 558 (1993).
[46] G. Kresse and J. Furthmüller, Comput. Mater. Sci. **6**, 15 (1996).
[47] J. P. Perdew, K. Burke, and M. Ernzerhof, Phys. Rev. Lett. **77**, 3865 (1996).
[48] G. Kresse and D. Joubert, Phys. Rev. B **59**, 1758 (1999).
[49] G. Kresse and J. Hafner, J. Phys.: Condens. Matter **6**, 8245 (1994).
[50] M. Methfessel and A. T. Paxton, Phys. Rev. B **40**, 3616 (1989).
[51] See Supplemental Material at http://link.aps.org/supplemental/10.1103/PhysRevMaterials.xx.xxxxxx for comparison of validation properties to EAM/MEAMs; more details regarding the calculation of nontypical lattice configurations are listed; equations for elastic constant calculations, and supporting figures/tables for the Mg surface segregation in Al-Mg alloys.
[52] A. Jain, S. P. Ong, G. Hautier, W. Chen, W. D. Richards, S. Dacek, S. Cholia, D. Gunter, D. Skinner, G. Ceder, and K. A. Persson, APL Mater. **1**, 011002 (2013).
[53] W. R. Tyson and W. A. Miller, Surf. Sci. **62**, 267 (1977).
[54] J. D. Cox, D. D. Wagman, V. A. Medvedev, and D. P. Wagman, *CODATA: Key Values for Thermodynamics* (Hemisphere Pub, New York, NY, 1989).
[55] A. S. Cooper, Acta Crystallogr. **15**, 578 (1962).
[56] W. Triftshäuser, Phys. Rev. B **12**, 4634 (1975).
[57] M. J. Fluss, L. C. Smedskjaer, M. K. Chason, D. G. Legnini, and R. W. Siegel, Phys. Rev. B **17**, 3444 (1978).
[58] R. Q. Hood, P R. C. Kent, and F. A. Reboredo, Phys. Rev. B **85**, 134109 (2012).
[59] R. Qiu, H. Lu, B. Ao, L. Huang, T. Tang, and P. Chen, Philos. Mag. **97**, 2164 (2017).
[60] G. N. Kamm and G. A. Alers, J. Appl. Phys. **35**, 327 (1964).
[61] M. Bauccio, *ASM Metals Reference Book* (ASM International, Hemisphere Pub, Ohio, 1993).
[62] C. Kittel and P. McEuen, *Introduction to Solid State Physics* (Wiley, New York, 1976), Vol. 8.
[63] F. W. Von Batchelder and R. F. Raeuchle, Phys. Rev. **105**, 59 (1957).
[64] P. Tzanetakis, J. Hillairet, and G. Revel, Phys. Status Solidi B **75**, 433 (1976).
[65] L. J. Slutsky and C. W. Garland, Phys. Rev. **107**, 972 (1957).
[66] S. Plimpton, J. Comput. Phys. **117**, 1 (1995).
[67] P. Hirel, Comput. Phys. Commun. **197**, 212 (2015).
[68] G. Henkelman and H. Jónsson, J. Chem. Phys. **113**, 9978 (2000).
[69] J. L. Whitton, Vacuum **33**, 367 (1983).
[70] S. M. Rassoulinejad-Mousavi and Y. Zhang, Sci. Rep. **8**, 2424 (2018).
[71] B. Jelinek, S. Groh, M. F. Horstemeyer, J. Houze, S.-G. Kim, G. J. Wagner, A. Moitra, and M. I. Baskes, Phys. Rev. B **85**, 245102 (2012).
[72] A. Hernandez, A. Balasubramanian, F. Yuan, S. A. M. Mason, and T. Mueller, Npj Comput. Mater. **5**, 112 (2019).
[73] C. A. Becker and M. Kramer, Modell. Simul. Mater. Sci. Eng. **18**, 074001 (2010).
[74] W. Gaasior, Z. Moser, and J. Pstruś, J. Phase Equilib. **21**, 167 (2000).
[75] T. Gancarz, J. Jourdan, W. Gasior, and H. Henein, J. Mol. Liq. **249**, 470 (2018).
[76] H. Okamoto, J. Phase Equilibria Diffus. **19**, 598 (1998).
[77] F. Berthier, B. Legrand, and G. Tréglia, Acta Mater. **47**, 2705 (1999).
[78] H. Deng, W. Hu, X. Shu, and B. Zhang, Appl. Surf. Sci. **221**, 408 (2004).
[79] C. Colinet, A. Pasturel, and P. Hicter, Calphad **9**, 71 (1985).
[80] C. Lea and C. Molinari, J. Mater. Sci. **19**, 2336 (1984).
[81] J. Bloch, D. J. Bottomley, J. G. Mihaychuk, H. M. van Driel, and R. S. Timsit, Surf. Sci. **322**, 168 (1995).
[82] Y. Liu, Y. Chen, and C. Yang, AIP Adv. **5**, 087147 (2015).
[83] M. Hoffmann and P. Wynblatt, Metall. Trans. A **20**, 215 (1989).
[84] N. Smith, B. Gleeson, W. A. Saidi, A. Kvithyld, and G. Tranell, Ind. Eng. Chem. Res. **58**, 1434 (2019).
[85] The training database and the potential are freely available at saidigroup.pitt.edu or by contacting the corresponding author.